Journal of Materials Chemistry C

ROYAL SOCIETY OF CHEMISTRY

PAPER

View Article Online
View Journal | View Issue

Cite this: J. Mater. Chem. C, 2023, 11, 14237

A SERS sensor based on 3D nanocone forests capable of intelligent classification of aquatic product dyes†

Yaqian Zhao,[ab] Ruoyang Huang,[ab] Xin Li,[ab] Xuanjiao Mao,[bc] Shaohang Xu,[ab] Na Zhou,[ab] Shaojuan Li,*[bd] Haiyang Mao *[ab] and Chengjun Huang [ab]

Received 29th June 2023,
Accepted 15th September 2023

DOI: 10.1039/d3tc02271d

rsc.li/materials-c

In this work, a novel surface-enhanced Raman scattering (SERS) sensor with high performance and capable of intelligent classification is developed for detection of prohibited dyes in aquatic products. The sensor is composed of nanocone forests (NCFs) grafted with gold (Au) nanoparticles (AuNPs), which are further attached with silver (Ag) NPs. The prepared 3D Ag-AuNPs@NCFs exhibit plasmonic hybridization modes, and thus are able to form enhanced electromagnetic fields, endowing the sensor with high sensitivity. The detection limit of this sensor for R6G is as low as 10^{-9} M, and the relative standard deviation is smaller than 6.84%. Based on this sensor, aquatic product dyes with concentrations lower than the limits of visual recognition are conveniently detected. Besides, with the assistance of a convolutional neural network model, the different dyes with coincident Raman peaks and similar colors are100% classified. These results indicate that such a 3D Ag-AuNPs@NCF-based SERS sensor has great potential in practical applications.

1. Introduction

In the aquaculture environment, bacteria and parasites are commonly found; however, their presence in excess may easily infect the aquaculture products and reduce production.[1–4] To address such an issue, it is necessary to use antibacterial drugs or pesticides. Nevertheless, in recent years, some aquaculture practitioners chose to use dyes such as crystalline violet (CV) and malachite green (MG), for they have stronger efficacy and can quickly kill bacteria and parasites.[3,5–7] On the other hand, the quality of aquatic products available to buy determines sales, and some vendors choose to add dye molecules such as methyl orange (MO), sunset yellow (SY) or tartrazine (TZ) in order to attract more customers.[8–10] However, all these dyes have adverse effects on human health, and thus are prohibited under normal circumstances. Traditionally, there are various methods that can detect dye residues in aquatic products, including the high-performance liquid chromatography (HPLC), thin-layer chromatography (TLC) and enzyme-linked immunosorbent assay (ELISA); however, these methods not only require complex pre-processing procedures but are also time-consuming and costly.[11–13] In this sense, it is urgent to develop a convenient, efficient, and low-cost technique for detecting aquatic dye residues.

Surface enhanced Raman spectroscopy (SERS) is a simple, low-cost, fast, ultra-sensitive and fingerprint analysis technology, which can provide identifiable vibration information for molecular recognition.[14–16] According to the working principle of the SERS technology, noble metal nanostructures are the prerequisites for all SERS devices, and between the adjacent nanostructures, the intensity of the local electromagnetic field can be strongly increased, forming "hot spots".[17–21] To simplify the preparation process and further improve the performance, nanostructures with different materials or morphologies can be prepared first. Afterwards, noble metal NPs are introduced on the nanostructures so that they are uniformly distributed on the surface of the structures.[22,23] Usually, noble metal NPs can be introduced on the nanostructures by magnetron sputtering and electron beam evaporation; however, these processing methods with high precision often require expensive and cutting-edge equipment.[24–27] On the other hand, nanoparticle assembly is a low-cost and simple way, which also provides new preparation ideas for SERS sensors.[28–30] So far, various assembly methods have been developed to immobilize AuNPs on different

[a] Institute of Microelectronics of Chinese Academy of Sciences, Beijing 100029, P. R. China. E-mail: maohaiyang@ime.ac.cn
[b] University of Chinese Academy of Sciences, Beijing 100049, P. R. China. E-mail: lishaojuan@ciomp.ac.cn
[c] The People's Hospital of Pingyang, Wenzhou 325499, P. R. China
[d] State Key Laboratory of Applied Optics, Changchun Institute of Optics Fine Mechanics and Physics, Chinese Academy of Sciences, Changchun 130033, P. R. China

† Electronic supplementary information (ESI) available. See DOI: https://doi.org/10.1039/d3tc02271d

substrates. For instance, the negatively charged NPs could be assembled on silicon wafers using positively charged aminopropyl triethoxysilane (APTMS) as an electrostatic linker.[31] However, this method usually suffers from the low coverage of the metal NPs. Assembling NPs using polyelectrolytes improves coverage, but produces more NP aggregation. Either the low coverage or the aggregation of NPs would reduce the performance of SERS sensors.[32] Therefore, it is necessary to develop an assembly method that can make the NPs disperse tightly while avoiding aggregation.

On the other hand, in practical applications involving aquatic product samples, SERS signals of certain dye molecules are usually characterized with a large number of other species; the spectra of these species may have high similarity, and their Raman peaks may overlap.[33–35] The manual classification of these Raman spectra is not only difficult, with low accuracy, but also greatly reduces the efficiency.[36] To overcome the specificity issues brought up by the similarity, some advanced algorithms, such as K-nearest neighbor, maximum likelihood method and support vector machine, have been established to classify the spectra. However, the traditional classification methods are usually accompanied by the curse of dimensionality, which often requires some dimensionality reduction methods for data processing in advance. Moreover, the data with reduced dimension are more likely to cause the problem of feature loss.[37,38] Therefore, an efficient and accurate model is urgently needed to automatically extract the characteristics of Raman data, and to achieve rapid and intelligent classification with high accuracy.

In this work, a 3D Ag-AuNPs@NCF-based SERS sensor is prepared using only a simple etching step and a block copolymer (BCP) brush template method. The performance of the device was verified by testing R6G, which shows a limit of detection (LOD) down to 10^{-9} M with a relative standard deviation (RSD) of less than 6.84% and enables qualitative detection of different dye molecules. In addition, with the help of a convolutional neural network (CNN) model, the device can quickly classify five different types of dye spectra with 100% accuracy. It is expected that this SERS sensor has promising applications in the field of food safety detection.

2. Experimental section

2.1. Materials

Silicon (Si) wafers were purchased from Research Materials Microtech Co., Ltd (Suzhou, China). Polyimide (PI) photoresist (ZKPI 5510L) was purchased from POME Technology Co., Ltd (Beijing, China). AuNPs (50 nm) were purchased from Longfei Biotechnology Co., Ltd (Shijiazhuang, China). PS-*b*-P4VP [M_n(PS) = 41 kg mol^{-1}, M_n(P4VP) = 20 kg mol^{-1}, M_w/M_n (total) = 1.18] was obtained from Polymer Source (Dorval, Canada). Tetrahydrofuran (THF), buffered hydrofluoric (BHF) acid were purchased from Sigma-Aldrich (Shanghai, China). R6G, CV, MG, MO, SY and TZ were purchased from J&K Scientific Ltd (Beijing, China). Deionized (DI) water (18.2 MΩ cm^{-1}) was used throughout the experiments. All chemicals were of reagent grade and were used without further purification. Organic filter membranes (1 μm) were purchased from Tianjin Jinteng Laboratory Equipment Co, Ltd (Tianjin, China). Samples of fishpond water were collected from local fish pond (Beijing, China) and a large yellow croaker was purchased from the local market (Beijing, China).

Two actual dye analytes were prepared with the sample of fishpond water. The aquaculture water samples were filtered three times with a membrane of 1 μm pore size to prepare MG solutions of different concentrations (10^{-5}–10^{-7} M). A squared sample with an area of 1 cm^2 was taken from the surface of the large yellow croaker, and the sample was immersed in a TZ solution with a concentration of 1×10^{-4} M (the EU standard is 1.9×10^{-4} M) for 15 min. Then, the TZ residues on the fish sample were collected by a cotton swab that was subsequently immersed and sonicated in an ethanol solution (2 mL) to dissolve the TZ molecules.

2.2. Fabrication of the SERS sensor

The preparation process (Fig. S1, ESI†) for the Si NCFs has been presented in detail in our previous article.[39] Briefly, the PI photoresist film spin-coated on the surface of silicon substrate is treated with oxygen and argon plasma to form nanowire forests (NWFs). In a subsequent anisotropic Si etching process, the NWFs act as masks to obtain Si NCFs. Later on, the residual NWFs are removed using BHF acid by wet etching.

With the Si NCFs, the 3D Ag-AuNPs@NCF-based SERS sensor is prepared according to the method shown in Fig. 1. Firstly, the prepared Si NCFs were immersed in a THF solution containing PS-*b*-P4VP for ten minutes to form a brush-like layer. After that, the Si NCFs rinsed with DI water were incubated in AuNPs solution for 12 h. The substrates with AuNPs@NCFs were then cleaned by DI water. Finally, Ag NPs (5 nm, deposition rate = 0.3 Å s^{-1}) were deposited on the substrate using an electron beam evaporation system (10 kV, 7×10^{-5} Pa) to form the SERS sensor with Ag-AuNPs@NCFs.

2.3. Characterization of the sensor and SERS measurements

The structure of the prepared Ag-AuNPs@NCF structure was investigated by scanning electron microscopy (SEM) (S-5500, Hitachi, Japan). Raman spectra were collected by a confocal Raman microscope equipped (inVia Reflex, Gloucestershire, UK) with a 632.8 nm laser source. During the measurements we used a 50× objective, with an effective laser intensity of 1.7 mW and an integration time of 10 s. During the test, 4 μL of the analyte solution was added dropwise to the fabricated SERS sensor (0.5 cm × 0.5 cm) and dried naturally at room temperature. All Raman spectra were acquired by the same method for subsequent analysis of the results. After the measurement, a baseline correction operation was performed on the unprocessed spectra using specialized analysis software (Wire 5.1).

2.4. Construction of a CNN classifier

Spectral preprocessing consisted of two primary steps. Firstly, asymmetric least squares smoothing (ALSS) was used for removing the background of the spectra, where the smoothing

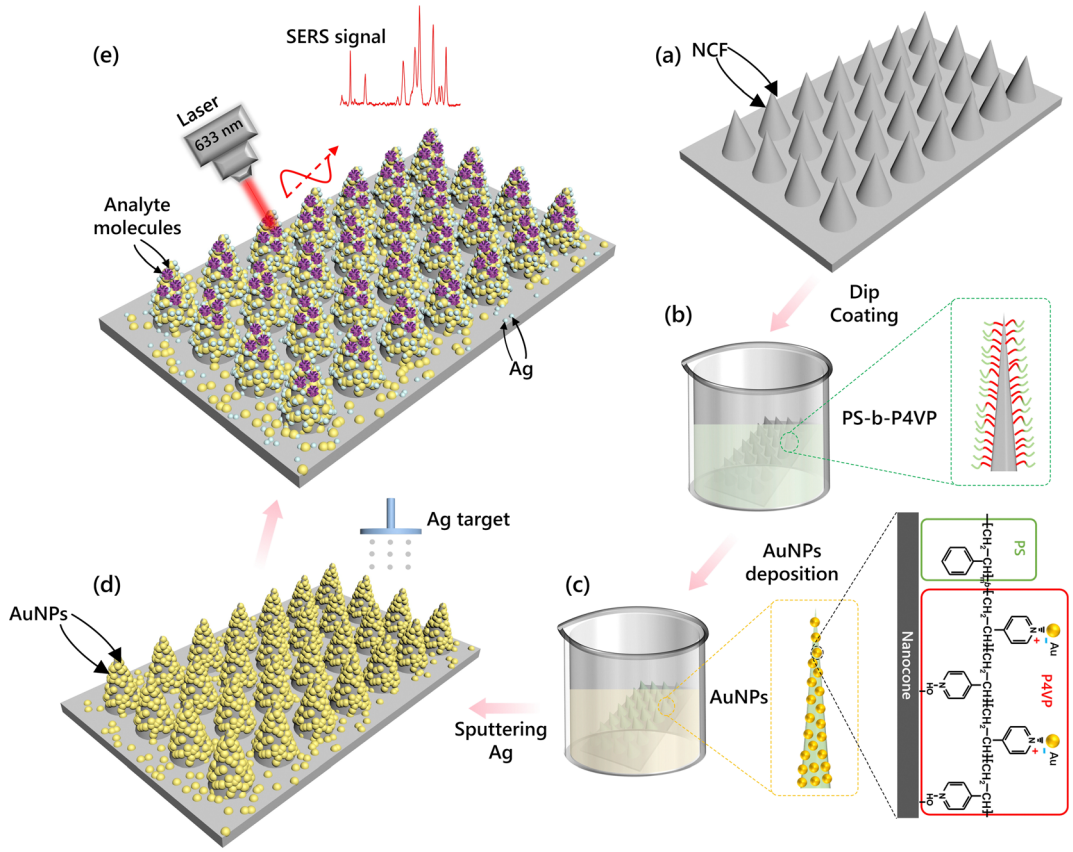

Fig. 1 Schematic diagram of the experiment to prepare Ag-AuNPs@NCF structure.

penalty coefficient and the asymmetry parameter were set at 105 and 0.001, respectively. Subsequently, the spectra after removing the background were smoothened (by Savitzky–Golay filtering algorithm) and normalized.

The Python programming language was used in all data processing. CNN was implemented using the PyTorch backend. We collected 1000 spectra using the prepared SERS sensors, and 200 for each dye. During the collection process, we changed the laser wavelength and solution concentrations, making the dataset more generalized. These were divided according to the proportion of training set (70%), validation set (20%), and independent test data set (10%). Among them, the independent

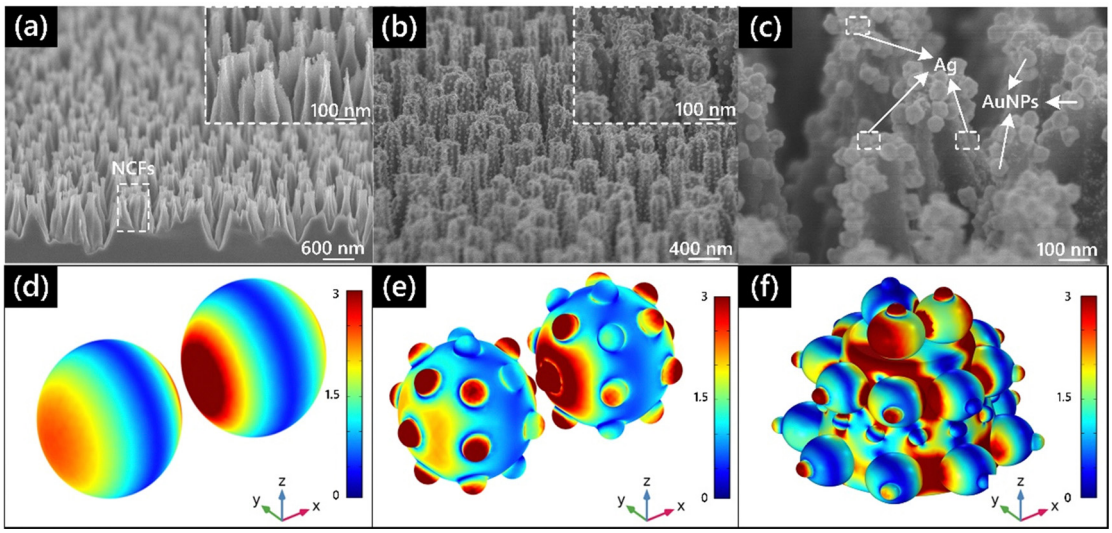

Fig. 2 SEM images of (a) Si NCFs, (b) AuNPs@NCFs, and (c) 3D Ag-AuNPs@NCFs. Simulation results of EM fields distributed on different structures: (d) the Au–Au NPs, (e) two adjacent AuNPs covered with AgNPs, and (f) The 3D Ag-AuNPs@NCFs.

test sets were used to verify the generalization ability of the model. Accuracy is considered as a measure for such a model performance and is calculated by dividing the number of correctly classified samples by the total number of samples.

3. Results and discussion

3.1. Characterization of SERS sensors

Fig. S2 (ESI†) illustrates SEM images of the NWFs; as is shown, the NWFs are composed of nanowires (NWs) with an average diameter of ~220 nm, an average spacing of ~600 nm, and an average height of ~5.7 μm. Composite nanostructures after Si etching are demonstrated in Fig. S3 (ESI†). The prepared composite nanostructures are composed of two layers, with NWFs as nanomasks on the top and with the NCFs directly under the NWFs. The structures after BHF wet etching are displayed in Fig. 2(a), where the NCs are with a height of ~1.2 μm, a bottom diameter around 200 nm, and a tilting angle around 80°. With such structural characteristics, the NCFs are able to provide a large specific surface area for capturing the assembled AuNPs.

A simple self-assembly method adopting a PS-*b*-P4VP BCP brush template was used to immobilize AuNPs on Si NCFs. Numerous hydrogen bonding points between the PS-*b*-P4VP and the Si NCFs allow for a stable and uniform BCP template. Since citrate capped AuNPs are negatively charged and P4VP is positively charged, AuNPs can electrostatically interact with P4VP to deposit on the BCP template. In fact, the density of AuNPs adsorbed on Si can be adjusted by changing the pH of the AuNP colloids. In the experiment, when the pH was around 4.5 (near the pK_a), the AuNPs immobilized on Si were uniformly and tightly distributed, while when the pH was decreased, the AuNPs piled up, aggregation of the nanoparticles became inevitable. As shown in Fig. S4(a) (ESI†), the distribution of AuNPs is quite uniform with a density of 140 NPs per μm^2 when the pH is 4.5, when the pH is 3.5, the density of AuNPs increases to 282 NPs per μm^2, but significant aggregation of the AuNPs takes place (Fig. S4(b), ESI†). Therefore, to achieve a better distribution, we immobilized the AuNPs on the Si NCFs at a pH value of 4.5. As shown in Fig. 2(b), the AuNPs are well distributed on the surface of the NCFs, forming the AuNPs@NCFs. Finally, with a sputtering step to attach Ag NPs to the surface of the AuNPs@NCFs, a 3D Ag-AuNPs@NCF-based SERS sensor was successfully prepared, as is demonstrated in Fig. 2(c). Meanwhile, Fig. S5 (ESI†) shows a SEM image of the 3D Ag-AuNPs@NCF-based SERS sensor. These images show Ag particles attached to the surface of the SERS sensor. That is to say, the sensor has a large number of strong ''hot spots'', and the plasma hybridization[40] effect between Ag and AuNPs results in extremely high SERS activity.

3.2. Electromagnetic (EM) enhancement mechanism

As is known, the ''hot spots'' originate from the sharpness of noble metal nanoparticles and the gaps between them. In the as-prepared 3D Ag-AuNPs@NCF-based SERS sensor, the gaps between the AuNPs as well as those between the AgNPs and AuNPs are in the nanometer scale, and therefore, a distribution of intense ''hot spots'' can be generated. As a proof of concept, the EM field distributions on different nanostructures were obtained through COMSOL Multiphysics simulations to evaluate the enhancement mechanism of the 3D Ag-AuNPs@NCF-based SERS sensor. A geometric model of Ag-AuNPs@NCF was established according to the actual morphology of the nanostructures shown in Fig. 2(c). In the simulation, the nanostructure was irradiated with a plane wave with a wavelength of 633 nm; here, the incident light propagated in the *Z* direction, and the electric field was along the *X* direction. The power density was 1 mW μm^{-2}, and the incident port properties of the light source were periodic. Since Fig. 2(d–e) only calculate the electromagnetic enhancement between two particles, the boundary condition was set to scattering boundary conditions. For Fig. 2(f), there is a NC structure in space at this point, so the boundary conditions were set to periodic boundary conditions with a Floquet period type and *k*-vector conditions from periodic light source ports. In the model shown in Fig. 2(d), the diameter of the AuNPs is 50 nm and the gap between them is 20 nm, respectively. The simulation results show the near-field coupling between the adjacent NPs enhances EM in a small range. This result indicates that the closely spaced AuNPs can provide EM enhancement to a certain extent. Then, after evaporation of AgNPs, the surface sharpness of the AuNPs is further increased by the bulges. As shown in Fig. 2(e), AgNPs with a diameter of 5 nm are distributed around the AuNPs, and the gaps between the AuNPs and AgNPs as well as the gaps inside the nanostructure contribute to a larger number of ''hot spots''. Moreover, the introduced Ag is able to generate a plasma hybridization effect with AuNPs, which produces a stronger electromagnetic enhancement effect.[39] Furthermore, for the practical structures shown in Fig. 2(c), a large EM enhancement is generated at the slits where the nanoparticles are distributed closely to each other; in addition, a large enhancement also emerges at the edge of the nanoparticles, as is demonstrated in Fig. 2(f). The simulation results verify that the 3D Ag-AuNPs@NCF-based SERS sensor has strong EM enhancement on the surface of the NCFs, which can greatly improve capability of SERS detection.

3.3. Performance of the 3D Ag-AuNPs@NCF-based SERS sensor

The performance of the SERS sensor was measured by using R6G molecules. As expected, such a sensor possesses high SERS activity, which can be attributed to the large number of ''hot spots'' with strong EM fields generated between the metal NPs, and to the plasmon hybridization effect of the bimetallic system. To further evaluate the SERS performance of the nanostructured, the 3D Ag-AuNPs@NCF sensor is compared with sensors based on AuNPs@Si and AuNPs@NCFs.

We dripped R6G solutions on different substrates and conducted SERS measurement after the solvent evaporation. Fig. 3(a) shows the SERS spectra of R6G obtained on different substrates. There are obvious characteristic peaks of R6G in the

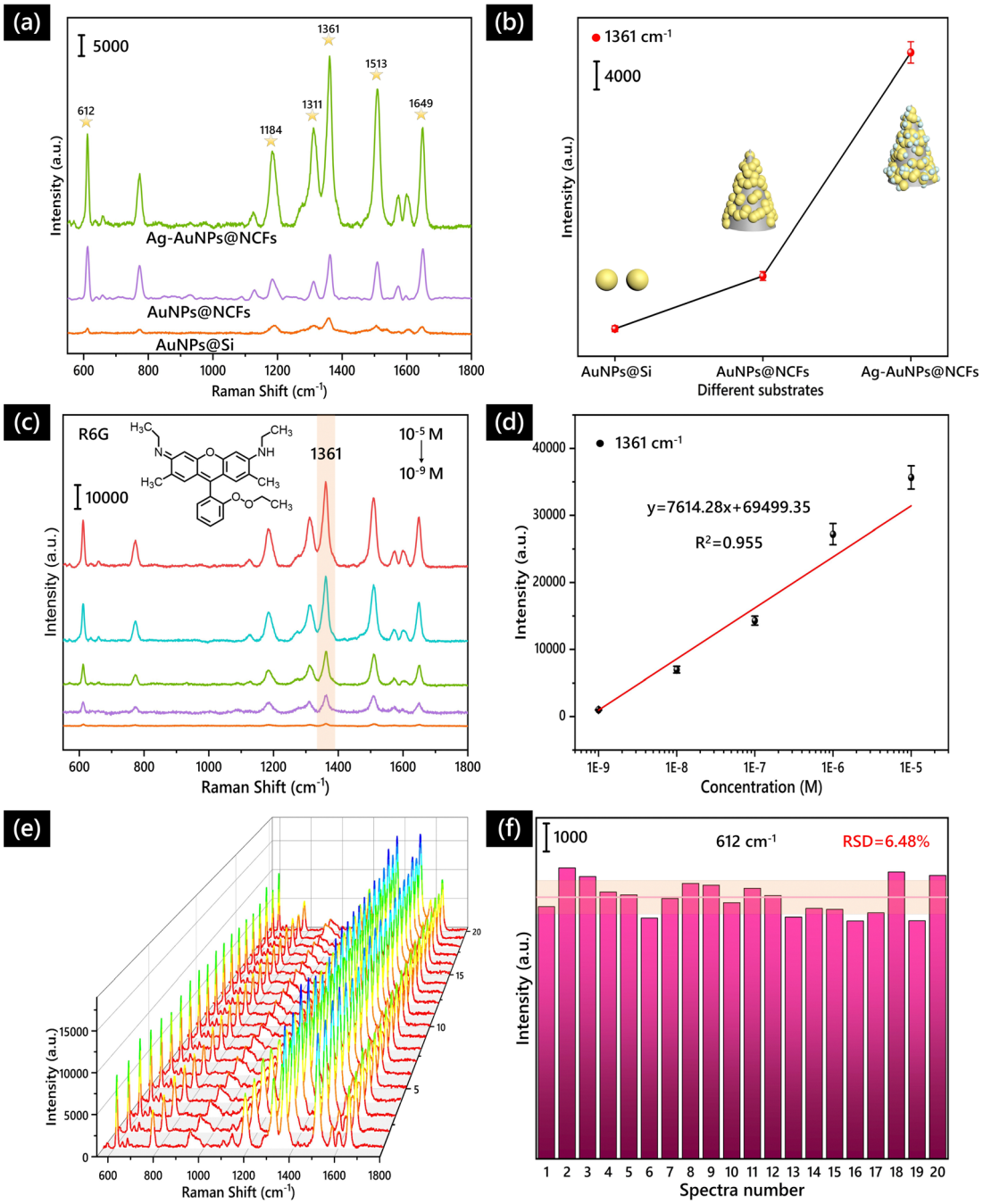

Fig. 3 (a) SERS spectra of 10^{-4} M R6G obtained on SERS substrates based on AuNPs@Si, AuNPs@NCFs and the 3D Ag-AuNPs@NCFs. (b) The intensities of the characteristic peaks at 1361 cm^{-1} of the three SERS spectra shown in (a), and the insets correspond to the schematic diagrams of the three structures. (c) SERS spectra of R6G solutions with concentration of 10^{-5}–10^{-9} M obtained on the 3D Ag-AuNPs@NCF-based sensor. (d) Calibration curve between the intensity of 1361 cm^{-1} characteristic peaks in the spectrum shown in (c), and the corresponding R6G concentration. (e) SERS spectra of 10^{-7} M R6G obtained at 20 randomly positions on the 3D Ag-AuNPs@NCF-based sensor. (f) The peak intensity at 612 cm^{-1} of the SERS spectra collected in (e).

three spectra, and the corresponding vibration attributions are listed in Table S1 (ESI†). Fig. 3(b) shows the peak intensities of the three Raman spectra at 1361 cm^{-1}, as can be observed, among the three substrates, the one based on the 3D Ag-AuNPs@NCFs shows the highest Raman signal intensity, which is because when compared with the other two competitors, such a structure has the largest surface area and can induce plasmon hybridization in two different noble metals, leading to the largest number of ''hot spots'' and the highest EM enhancement.

Then, the SERS spectra of R6G solutions with different concentrations (10^{-9}–10^{-5} M) were measured using different 3D Ag-AuNPs@NCF-based sensors, as shown in Fig. 3(c). The results demonstrate that the Raman intensity decreases with

the decreasing concentration, and the detectable limit concentration is 10^{-9} M. Fig. 3(d) shows the fitting results between the intensity of the Raman peak at 1361 cm^{-1} and the concentration of R6G; the calculated correlation coefficient is 0.955, which indicates that the 3D Ag-AuNPs@NCF-based sensor can perform a preliminary quantitative analysis of the detected analytes.

To investigate the sensitivity of the 3D Ag-AuNPs@NCF-based SERS device, the enhancement factor (EF) is calculated using the specific formula:[41]

$$EF = \frac{I_{SERS} \times N_{REF}}{I_{REF} \times N_{SERS}}$$

N_{SERS} and N_{REF} represent the molecular number of the detected substances on the two substrates, I_{SERS} and I_{REF} represent the intensities of the corresponding Raman spectral characteristic peaks. Fig. S6 (ESI†) shows a spectrum of 10^{-8} M R6G obtained

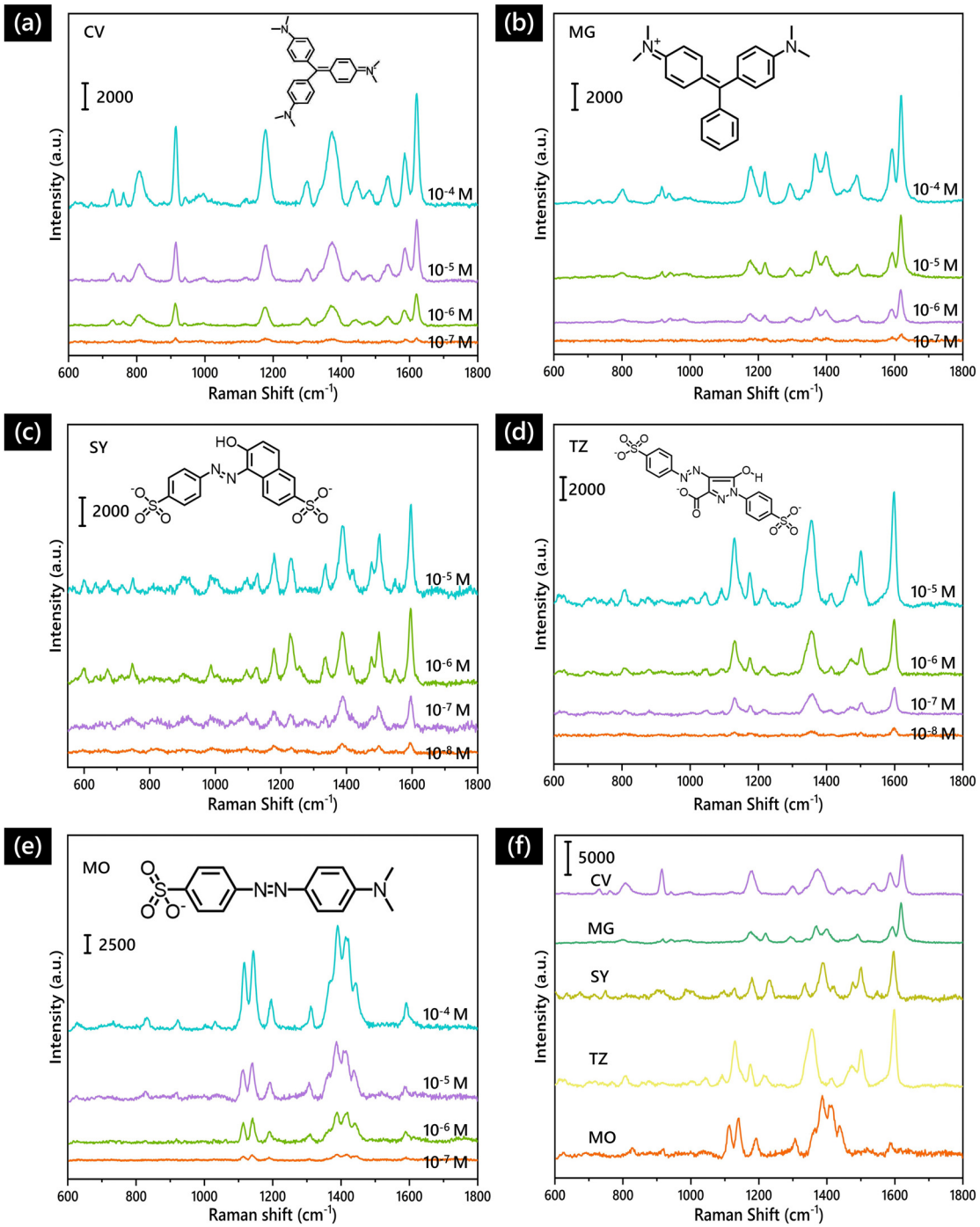

Fig. 4 (a)–(e) The SERS test results of five dye samples (CV, MG, SY, TZ and MO) with different molecular concentrations. (f) Raman spectra of CV (10^{-5} M), MG (10^{-5} M), SY (10^{-5} M), TZ (10^{-5} M) and MO (10^{-5} M).

from the 3D Ag-AuNPs@NCF-based sensor (red curve Fig. S6(a), ESI†) and reference spectrum of 10^{-2} M R6G obtained on the flat Si substrate (Fig. S6(b), ESI†). Table S2 (ESI†) shows the ratios of I_{SERS}/I_{REF} at 612, 1184, 1361 and 1649 cm^{-1}. Accordingly, a maximum EF of 1.89×10^6 is obtained (1649 cm^{-1}).

To evaluate repeatability of the 3D Ag-AuNPs@NCF-based sensor, 20 SERS spectra of 10^{-7} M R6G were obtained at different positions of the same sensor, as shown in Fig. 3(e). The intensities at characteristic peaks of 612, 1184, 1361 and 1649 cm^{-1} in the 20 spectra are illustrated in Fig. 3(f) and Fig. S7 (ESI†). The corresponding relative standard deviations (RSDs) at 612, 1184, 1361 and 1649 cm^{-1} are calculated to be 6.84%, 5.80%, 5.93% and 6.46%, respectively. Meanwhile, we tested three SERS spectra using five different sensors, and the signal intensity at the characteristic peak of 612 cm^{-1} in each spectrum was selected for calculation and analysis. As shown in Fig. S8 (ESI†), the signal intensities of the spectra obtained from different SERS sensors ranged from 8500 to 10 000 with RSDs of 6.71%, 6.42%, 7.15%, 5.9% and 7.31%, respectively. These results indicate that the 3D Ag-AuNPs@NCF-based sensor is highly reproducible, which makes it attractive for practical applications.

3.4. Applications of the 3D Ag-AuNPs@NCF-based SERS sensor

3.4.1. Detection of dye solutions. Five dyes (including CV, MG, SY, TZ and MO) commonly used in aquatic products were detected using the 3D Ag-AuNPs@NCF-based sensor. Fig. 4(a)–(e) show the SERS spectra and corresponding molecular structures of the five dyes. Each dye molecule has corresponding multiple characteristic peaks, and the vibration properties corresponding to different characteristic peaks are listed in Table S3 (ESI†), the

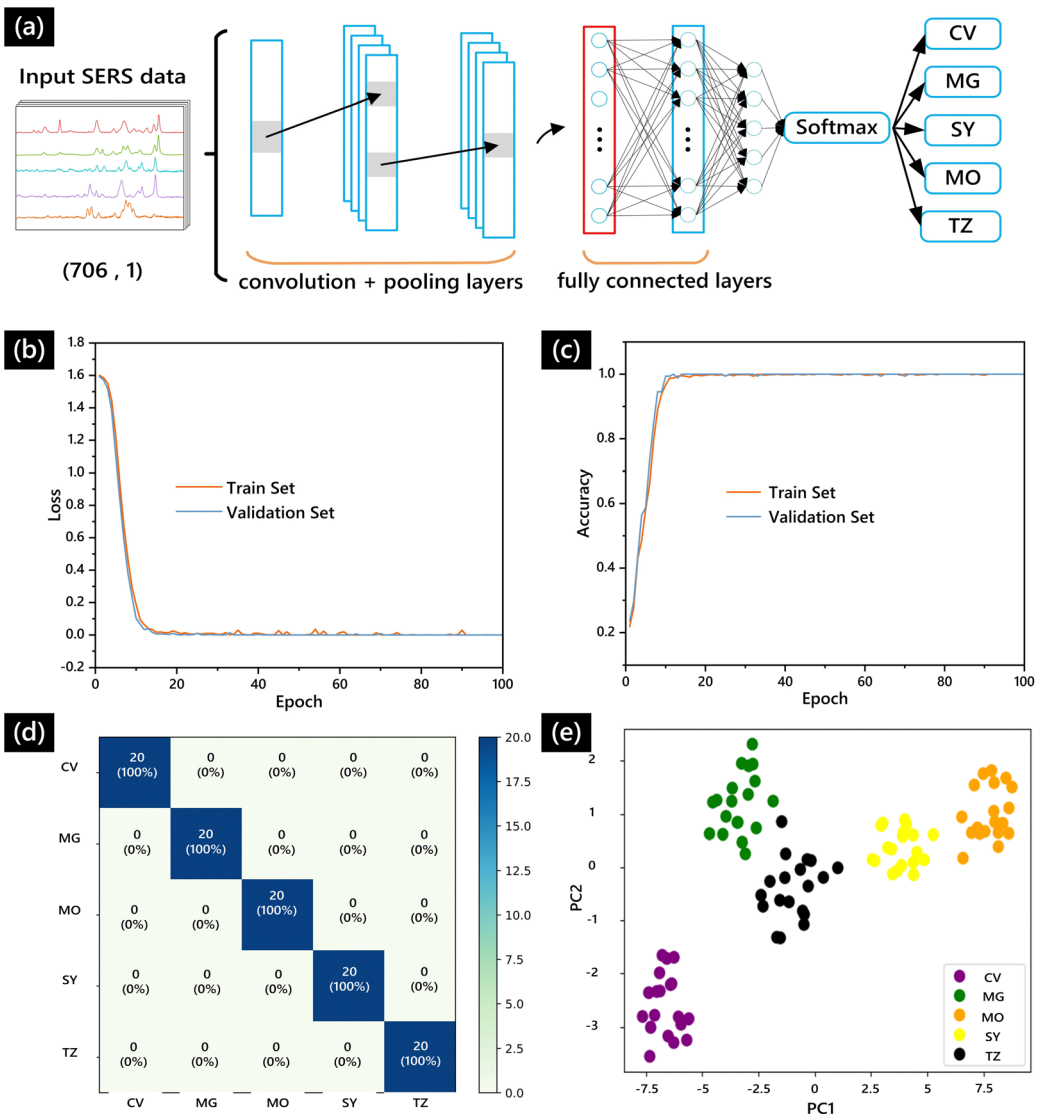

Fig. 5 Classification of dye SERS spectra using the CNN model. (a) CNN model architecture is trained using the spectra of the five dyes. (b) Loss and (c) accuracy evolution during the CNN training and validation. (d) Confusion matrix of the constructed CNN classifier tested with the independent test dataset. (e) The output probability vector is projected into 2D space, and the feature differentiation is colored according to the real labels of the spectrum.

detection limits are recorded in Table S4 (ESI†). When the solution concentration is as low as 10^{-7} M, at which the dye solution is below the visual recognition limit, the 3D Ag-AuNPs@NCF-based sensor can still detect the Raman signals of these dyes. The Raman spectra of CV, MG, SY, TZ and MO shown in Fig. 4(f) directly illustrate the differences between the characteristic peaks of the different dye molecules, and the difference in the number and position of these characteristic peaks can be used as a criterion for qualitative detection of the dyes. However, different dye molecules have structural similarities, some characteristic peaks in the spectra are very close or even overlapped, such as 1591 and 1619 cm^{-1} of MG, 1585 and 1621 cm^{-1} of CV, 1597 cm^{-1} of TZ and 1596 cm^{-1} of SY. To efficiently classify and distinguish these five types of dye, a CNN model was used to establish a classifier.

3.4.2. Intelligent classification of dye spectra. CNN has achieved significant success in recognizing similar data. Thereby, in this work, we choose CNN to process the data of SERS spectra from single dyes and to classify them. The training of the CNN model is an iterative process in which the network parameters are updated based on the training data to achieve the minimization of the loss associated with the prediction class labels and the true class labels. The structure of the CNN used to implement spectral classification is shown in Fig. 5(a). The SERS spectra with a length of 706 are used to serve as the input layer of the CNN, and also includes three convolutional layers, two maximum pooling layers and three fully connected layers. The specific parameters of the designed CNN model are shown in Table S5 (ESI†). The outputs of the CNN model are concatenated in a 1D feature vector, which is passed to the fully connected classifier with the SoftMax activation function, giving the probability that the input belongs to a particular class (dye) of samples. When training is completed, information about the parameters related to this model can be stored for subsequent use. The stored network contains multiple hidden layers for automatic extraction of SERS spectral data, avoiding manual extraction of spectral features.

The training progress of the constructed CNN model is shown in Fig. 5(b). The CNN model converges rapidly in a very short training cycle and the prediction loss decreases dramatically, indicating that the CNN model achieves the desired classification performance. Similarly, as shown in Fig. 5(c), the trend of the model prediction accuracy is consistent with the trend of the loss function, achieving a convergence around the tenth epoch. In order to transmit the complete data set in the same neural network for many times, the whole training process was continued to reach 100 epochs to prove the convergence of the model. Overall, at the end of the training process, the average validation loss and validation accuracy

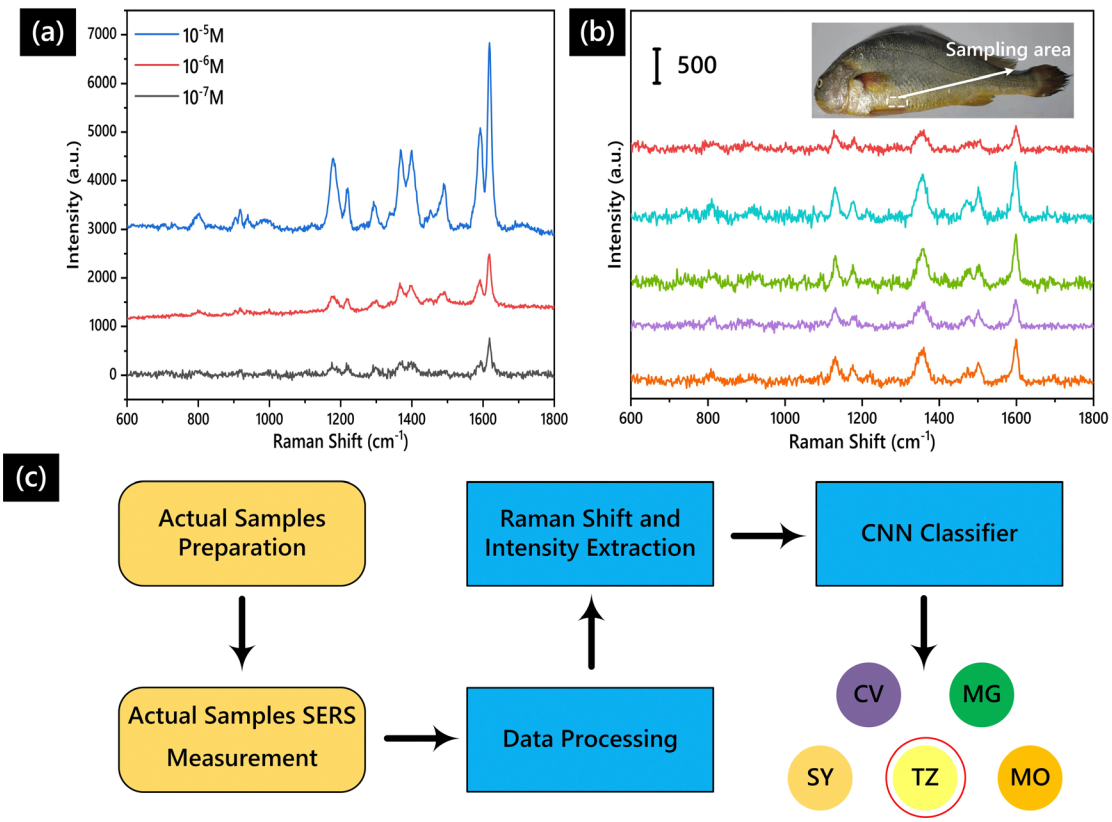

Fig. 6 SERS detection of dyes in aquaculture water samples. (a) Raman spectra of MG (10^{-5}-10^{-7} M) dissolved in fishpond water measured with the as-prepared sensor. (b) Five groups of TZ Raman spectra obtained from the real fish sample. (c) A CNN model-based method for classifying measurement results of actual samples.

between the last 10 epochs are 1.59×10^{-5} and 1.0, respectively, which can be considered as fully converged. As shown in the confusion plot in Fig. 5(d), to validate the performance of the constructed CNN classifier in real applications, an independent test set was used for evaluation, and the final test accuracy was 100%.

For better visualization, the output of the CNN is downscaled, and the results are projected into a 2D space. As shown in Fig. 5(e), each color in 2D space represents a different spectral class, and the different points show the characteristic differences of the dye spectra after CNN processing. These feature regions are completely separated, suggesting that the CNN has successfully distinguished the dye spectra with similarity.

3.4.3. Detection of aquaculture water samples. To test the practicability of the developed 3D Ag-AuNPs@NCF-based sensor in a realistic application, we detected the existence of the dyes in actual samples. As proof of concept, we prepared two actual samples in advance, namely the MG solution using fishpond water as the solvent, and the TZ solution obtained from the surface of large yellow croaker. The measurement results of the actual samples are shown in Fig. 6(a) and (b). The spectra of MG molecules in the aquaculture water samples have characteristic peaks consistent with those of MG. Meanwhile, the overall signals from the real fish sample are weak, but the distinctive spectral profile and peak intensities of the TZ molecules can be discerned.

From these preliminary testing results, the 3D Ag-AuNPs@NCF-based sensor can effectively identify the presence of dye molecules despite complex components in the samples as they are very similar with the actual environment. In order to verify the accuracy of the CNN model for the classification of the actual spectra, we followed the steps shown in Fig. 6(c) for further testing and analyzing the TZ spectra obtained in Fig. 6(b). The results show that the measured spectra of the two actual samples can be correctly classified.

4. Conclusions

In this work, a 3D Ag-AuNPs@NCF-based SERS sensor with high sensitivity was prepared based on a facile preparation process for nanoforests and metal NPs. The surface plasmonic hybridization in the nanostructures allowed the sensor to achieve a detection limit of 10^{-9} M and an enhancement factor of 1.89×10^{6}; besides, the uniformly distributed AuNPs helped the sensor to have good reproducibility (RSD $<$ 6.84%). In addition, with the 3D Ag-AuNPs@NCF-based SERS sensor, five different dyes with trace concentrations were detected, and assisted using a CNN model, and automatic classification of these dyes was realized with a 100% accuracy. Furthermore, offending dyes in aquaculture samples as well as in real fish samples were also detected. These results indicate that the prepared 3D SERS sensor has promising applications in aquatic product safety detection.

Conflicts of interest

There are no conflicts to declare.

Acknowledgements

This work was supported in part by the National Natural Science Foundation of China (Grant No. 62022081, 62201567 and 61974099), the Science Fund for Creative Research Groups of the National Natural Science Foundation of China (No. 62121005), the Youth Innovation Promotion Association, Chinese Academy of Sciences (Grant No. 2018153 and 2022117), and the Key-Area Research and Development Program of Guangdong Province (Grant No. 2019B010117001).

References

1 F. Chen, Y. Zhao, S. Zhang, S. Wei, A. Ming and C. Mao, Hydrophobic Wafer-Scale High-Reproducibility SERS Sensor Based on Silicon Nanorods Arrays Decorated with Au Nanoparticles for Pesticide Residue Detection, *Biosensors*, 2022, **12**, 273.
2 L. He, N. J. Kim, H. Li, Z. Hu and M. Lin, Use of a fractal-like gold nanostructure in surface-enhanced Raman spectroscopy for detection of selected food contaminants, *J. Agric. Food Chem.*, 2008, **56**, 9843–9847.
3 L. Li and W. S. Chin, Rapid Fabrication of a Flexible and Transparent Ag Nanocubes@PDMS Film as a SERS Substrate with High Performance, *ACS Appl. Mater. Interfaces*, 2020, **12**, 37538–37548.
4 N. Singh, J. Prakash, M. Misra, A. Sharma and R. K. Gupta, Dual Functional Ta-Doped Electrospun TiO(2) Nanofibers with Enhanced Photocatalysis and SERS Detection for Organic Compounds, *ACS Appl. Mater. Interfaces*, 2017, **9**, 28495–28507.
5 S. Kim, J.-H. Joo, W. Kim, A. Bang, H. W. Choi, S. W. Moon and S. Choi, A facile, portable surface-enhanced Raman spectroscopy sensing platform for on-site chemometrics of toxic chemicals, *Sens. Actuators, B*, 2021, **343**, 130102.
6 Y. Liu, L. Lei, Y. Wu, Y. Chen, J. Yan, W. Zhu, X. Tan and Q. Wang, Fabrication of sea urchin-like Au@SiO_2 nanoparticles SERS substrate for the determination of malachite green in tilapia, *Vib. Spectrosc.*, 2022, **118**, 103319.
7 M. Zhang, H. Sun, X. Chen, J. Yang, L. Shi, T. Chen, Z. Bao, J. Liu and Y. Wu, Highly Efficient Photoinduced Enhanced Raman Spectroscopy (PIERS) from Plasmonic Nanoparticles Decorated 3D Semiconductor Arrays for Ultrasensitive, Portable, and Recyclable Detection of Organic Pollutants, *ACS Sens.*, 2019, **4**, 1670–1681.
8 H. Liu, P. Zhao, Y. Wang, S. Li, L. Zhang, Y. Zhang, S. Ge and J. Yu, Paper-based sandwich type SERS sensor based on silver nanoparticles and biomimetic recognizer, *Sens. Actuators, B*, 2020, **313**, 127989.
9 B. P. Majee Bhawna and A. K. Mishra, Bi-functional ZnO nanoparticles as a reusable SERS substrate for nano-molar detection of organic pollutants, *Mater. Res. Express*, 2020, **6**, 1250j1251.
10 M. Zhang, T. Chen, Y. Liu, J. Zhang, H. Sun, J. Yang, J. Zhu, J. Liu and Y. Wu, Plasmonic 3D Semiconductor-Metal Nanopore Arrays for Reliable Surface-Enhanced Raman

Scattering Detection and In-Site Catalytic Reaction Monitoring, *ACS Sens.*, 2018, **3**, 2446–2454.

11 C. Wang, C. Wang, X. Wang, K. Wang, Y. Zhu, Z. Rong, W. Wang, R. Xiao and S. Wang, Magnetic SERS Strip for Sensitive and Simultaneous Detection of Respiratory Viruses, *ACS Appl. Mater. Interfaces*, 2019, **11**, 19495–19505.

12 Y. J. Ai, P. Liang, Y. X. Wu, Q. M. Dong, J. B. Li, Y. Bai, B. J. Xu, Z. Yu and D. Ni, Rapid qualitative and quantitative determination of food colorants by both Raman spectra and Surface-enhanced Raman Scattering (SERS), *Food Chem.*, 2018, **241**, 427–433.

13 Y. S. Chien, C. W. Chang and C. C. Huang, Differential surface partitioning for an ultrasensitive solid-state SERS sensor and its application to food colorant analysis, *Food Chem.*, 2022, **383**, 132415.

14 L. Ma, Y. L. Chen, X. P. Song, D. J. Yang, H. X. Li, S. J. Ding, L. Xiong, P. L. Qin and X. B. Chen, Structure-Adjustable Gold Nanoingots with Strong Plasmon Coupling and Magnetic Resonance for Improved Photocatalytic Activity and SERS, *ACS Appl. Mater. Interfaces*, 2020, **12**, 38554–38562.

15 D. Huo, B. Chen, G. Meng, Z. Huang, M. Li and Y. Lei, Ag-Nanoparticles@Bacterial Nanocellulose as a 3D Flexible and Robust Surface-Enhanced Raman Scattering Substrate, *ACS Appl. Mater. Interfaces*, 2020, **12**, 50713–50720.

16 W. Wang, S. Pu, W. Hu, J. Gu, B. Ren, Z. Tian and G. Liu, Revealing the synergistic effect of capillary force and electrostatic attraction for D-SERS sensitivity, *Chem. Commun.*, 2022, **58**, 3953–3956.

17 J. P. Fraser, P. Postnikov, E. Miliutina, Z. Kolska, R. Valiev, V. Svorcik, O. Lyutakov, A. Y. Ganin and O. Guselnikova, Application of a 2D Molybdenum Telluride in SERS Detection of Biorelevant Molecules, *ACS Appl. Mater. Interfaces*, 2020, **12**, 47774–47783.

18 Y. C. Kao, X. Han, Y. H. Lee, H. K. Lee, G. C. Phan-Quang, C. L. Lay, H. Y. F. Sim, V. J. X. Phua, L. S. Ng, C. W. Ku, T. C. Tan, I. Y. Phang, N. S. Tan and X. Y. Ling, Multiplex Surface-Enhanced Raman Scattering Identification and Quantification of Urine Metabolites in Patient Samples within 30 min, *ACS Nano*, 2020, **14**, 2542–2552.

19 X. Liu, S. Yang, Y. Li, B. Wang, J. Guo and X. Ma, Mesoporous Nanostructures Encapsulated with Metallic Nanodots for Smart SERS Sensing, *ACS Appl. Mater. Interfaces*, 2021, **13**, 186–195.

20 W. Shan, R. Liu, H. Zhao, Z. He, Y. Lai, S. Li, G. He and J. Liu, In Situ Surface-Enhanced Raman Spectroscopic Evidence on the Origin of Selectivity in CO(2) Electrocatalytic Reduction, *ACS Nano*, 2020, **14**, 11363–11372.

21 J. Song, W. Cheng, M. Nie, X. He, W. Nam, J. Cheng and W. Zhou, Partial Leidenfrost Evaporation-Assisted Ultrasensitive Surface-Enhanced Raman Spectroscopy in a Janus Water Droplet on Hierarchical Plasmonic Micro-/Nanostructures, *ACS Nano*, 2020, **14**, 9521–9531.

22 S. Lee and I. Choi, Fabrication Strategies of 3D Plasmonic Structures for SERS, *BioChip J.*, 2019, **13**, 30–42.

23 A. X. Wang and X. Kong, Review of Recent Progress of Plasmonic Materials and Nano-Structures for Surface-Enhanced Raman Scattering, *Materials*, 2015, **8**, 3024–3052.

24 J. Wang, K. M. Koo, Y. Wang and M. Trau, Engineering State-of-the-Art Plasmonic Nanomaterials for SERS-Based Clinical Liquid Biopsy Applications, *Adv. Sci.*, 2019, **6**, 1900730.

25 J. Langer, D. Jimenez de Aberasturi, J. Aizpurua, R. A. Alvarez-Puebla, B. Auguie, J. J. Baumberg, G. C. Bazan, S. E. J. Bell, A. Boisen, A. G. Brolo, J. Choo, D. Cialla-May, V. Deckert, L. Fabris, K. Faulds, F. J. Garcia de Abajo, R. Goodacre, D. Graham, A. J. Haes, C. L. Haynes, C. Huck, T. Itoh, M. Kall, J. Kneipp, N. A. Kotov, H. Kuang, E. C. Le, Ru, H. K. Lee, J. F. Li, X. Y. Ling, S. A. Maier, T. Mayerhofer, M. Moskovits, K. Murakoshi, J. M. Nam, S. Nie, Y. Ozaki, I. Pastoriza-Santos, J. Perez-Juste, J. Popp, A. Pucci, S. Reich, B. Ren, G. C. Schatz, T. Shegai, S. Schlucker, L. L. Tay, K. G. Thomas, Z. Q. Tian, R. P. Van Duyne, T. Vo-Dinh, Y. Wang, K. A. Willets, C. Xu, H. Xu, Y. Xu, Y. S. Yamamoto, B. Zhao and L. M. Liz-Marzan, Present and Future of Surface-Enhanced Raman Scattering, *ACS Nano*, 2020, **14**, 28–117.

26 C. D. L. de Albuquerque, K. M. Hokanson, S. R. Thorud, R. G. Sobral-Filho, N. C. Lindquist and A. G. Brolo, Dynamic Imaging of Multiple SERS Hotspots on Single Nanoparticles, *ACS Photonics*, 2020, **7**, 434–443.

27 D. Paria, K. S. Kwok, P. Raj, P. Zheng, D. H. Gracias and I. Barman, Label-Free Spectroscopic SARS-CoV-2 Detection on Versatile Nanoimprinted Substrates, *Nano Lett.*, 2022, **22**, 3620–3627.

28 Z. Huang, X. Lei, Y. Liu, Z. Wang, X. Wang, Z. Wang, Q. Mao and G. Meng, Tapered Optical Fiber Probe Assembled with Plasmonic Nanostructures for Surface-Enhanced Raman Scattering Application, *ACS Appl. Mater. Interfaces*, 2015, **7**, 17247–17254.

29 Y. Ma, D. Sikdar, A. Fedosyuk, L. Velleman, D. J. Klemme, S. H. Oh, A. R. J. Kucernak, A. A. Kornyshev and J. B. Edel, Electrotunable Nanoplasmonics for Amplified Surface Enhanced Raman Spectroscopy, *ACS Nano*, 2020, **14**, 328–336.

30 X. Li, F. Wang, X. Wang, W. Zhao, H. Liu, M. Li, Y. Zhao, L. Zhang and C. Huang, Plasmonic-photonic hybrid configuration on optical fiber tip: Toward low-cost and miniaturized biosensing probe, *Sens. Actuators, B*, 2022, **367**, 132059.

31 J. Chen, S. Shi, R. Su, W. Qi, R. Huang, M. Wang, L. Wang and Z. He, Optimization and application of reflective LSPR optical fiber biosensors based on silver nanoparticles, *Sensors*, 2015, **15**, 12205–12217.

32 M. Lu, H. Zhu, C. G. Bazuin, W. Peng and J. F. Masson, Polymer-Templated Gold Nanoparticles on Optical Fibers for Enhanced-Sensitivity Localized Surface Plasmon Resonance Biosensors, *ACS Sens.*, 2019, **4**, 613–622.

33 N. Cheng, D. Chen, B. Lou, J. Fu and H. Wang, A biosensing method for the direct serological detection of liver diseases by integrating a SERS-based sensor and a CNN classifier, *Biosens. Bioelectron.*, 2021, **186**, 113246.

34 M. Erzina, A. Trelin, O. Guselnikova, B. Dvorankova, K. Strnadova, A. Perminova, P. Ulbrich, D. Mares,

V. Jerabek, R. Elashnikov, V. Svorcik and O. Lyutakov, Precise cancer detection via the combination of functionalized SERS surfaces and convolutional neural network with independent inputs, *Sens. Actuators, B*, 2020, **308**, 127660.

35 X. Lin, D. Lin, Y. Chen, J. Lin, S. Weng, J. Song and S. Feng, High Throughput Blood Analysis Based on Deep Learning Algorithm and Self-Positioning Super-Hydrophobic SERS Platform for Non-Invasive Multi-Disease Screening, *Adv. Funct. Mater.*, 2021, **31**, 2103382.

36 L. Kong, J. Chen and M. Huang, GO/Au@Ag nanobones decorated membrane for simultaneous enrichment and on-site SERS detection of colorants in beverages, *Sens. Actuators, B*, 2021, **344**, 130163.

37 X. Shao, H. Zhang, Y. Wang, H. Qian, Y. Zhu, B. Dong, F. Xu, N. Chen, S. Liu, J. Pan and W. Xue, Deep convolutional neural networks combine Raman spectral signature of serum for prostate cancer bone metastases screening, *Nanomedicine*, 2020, **29**, 102245.

38 Q. Fu, Y. Zhang, P. Wang, J. Pi, X. Qiu, Z. Guo, Y. Huang, Y. Zhao, S. Li and J. Xu, Rapid identification of the resistance of urinary tract pathogenic bacteria using deep learning-based spectroscopic analysis, *Anal. Bioanal. Chem.*, 2021, **413**, 7401–7410.

39 R. Li, H. Mao, M. Shi, Q. Zhao, D. Chen and J. Xiong, Parahydrophobic 3D nanohybrid substrates with two pathways of molecular enrichment and multilevel plasmon hybridization, *Sens. Actuators, B*, 2020, **320**, 128357.

40 M. Li, M. Shi, B. Wang, C. Zhang, S. Yang, Y. Yang, N. Zhou, X. Guo, D. Chen, S. Li, H. Mao and J. Xiong, Quasi-Ordered Nanoforests with Hybrid Plasmon Resonances for Broadband Absorption and Photodetection, *Adv. Funct. Mater.*, 2021, **31**, 2102840.

41 X. Jin, Q. Zhu, L. Feng, X. Li, H. Zhu, H. Miao, Z. Zeng, Y. Wang, Y. Li, L. Wang, X. Liu and G. Shi, Light-Trapping SERS Substrate with Regular Bioinspired Arrays for Detecting Trace Dyes, *ACS Appl. Mater. Interfaces*, 2021, **13**, 11535–11542.